

See discussions, stats, and author profiles for this publication at: <https://www.researchgate.net/publication/278731149>

# Air Stable Doping and Intrinsic Mobility Enhancement in Monolayer Molybdenum Disulfide by Amorphous Titanium Suboxide Encapsulation

ARTICLE *in* NANO LETTERS · JUNE 2015

Impact Factor: 13.59 · DOI: 10.1021/acs.nanolett.5b00314 · Source: PubMed

CITATIONS

2

READS

65

15 AUTHORS, INCLUDING:



**Amritesh Rai**

University of Texas at Austin

17 PUBLICATIONS 34 CITATIONS

SEE PROFILE



**Anupam Roy**

University of Texas at Austin

42 PUBLICATIONS 121 CITATIONS

SEE PROFILE



**Rudresh Ghosh**

University of North Carolina at Chapel Hill

19 PUBLICATIONS 200 CITATIONS

SEE PROFILE



**Emanuel Tutuc**

University of Texas at Austin

211 PUBLICATIONS 7,518 CITATIONS

SEE PROFILE

# Air Stable Doping and Intrinsic Mobility Enhancement in Monolayer Molybdenum Disulfide by Amorphous Titanium Suboxide Encapsulation

Amritesh Rai,<sup>\*,†</sup> Amithraj Valsaraj,<sup>†</sup> Hema C.P. Movva,<sup>†</sup> Anupam Roy,<sup>†</sup> Rudresh Ghosh,<sup>†</sup> Sushant Sonde,<sup>†</sup> Sangwoo Kang,<sup>†</sup> Jiwon Chang,<sup>‡</sup> Tanuj Trivedi,<sup>†</sup> Rik Dey,<sup>†</sup> Samareesh Guchhait,<sup>†</sup> Stefano Larentis,<sup>†</sup> Leonard F. Register,<sup>†</sup> Emanuel Tutuc,<sup>†</sup> and Sanjay K. Banerjee<sup>†</sup>

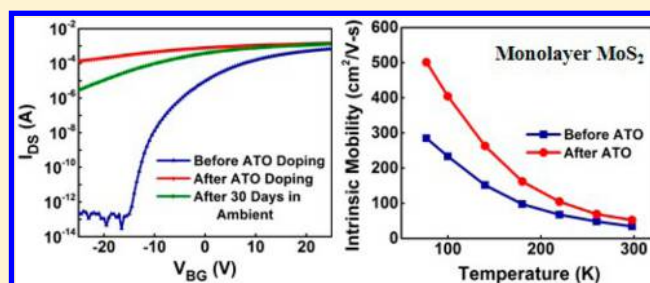
<sup>†</sup>Microelectronics Research Center and Department of Electrical and Computer Engineering, The University of Texas at Austin, Austin, Texas 78758, United States

<sup>‡</sup>SEMATECH, 257 Fuller Rd #2200, Albany, New York-12203, United States

## S Supporting Information

**ABSTRACT:** To reduce Schottky-barrier-induced contact and access resistance, and the impact of charged impurity and phonon scattering on mobility in devices based on 2D transition metal dichalcogenides (TMDs), considerable effort has been put into exploring various doping techniques and dielectric engineering using high- $\kappa$  oxides, respectively. The goal of this work is to demonstrate a high- $\kappa$  dielectric that serves as an effective n-type charge transfer dopant on monolayer (ML) molybdenum disulfide ( $\text{MoS}_2$ ). Utilizing amorphous titanium suboxide (ATO) as the “high- $\kappa$  dopant”, we achieved a contact resistance of  $\sim 180 \, \Omega \cdot \mu\text{m}$  that is the lowest reported value for ML  $\text{MoS}_2$ . An ON current as high as  $240 \, \mu\text{A}/\mu\text{m}$  and field effect mobility as high as  $83 \, \text{cm}^2/\text{V}\cdot\text{s}$  were realized using this doping technique. Moreover, intrinsic mobility as high as  $102 \, \text{cm}^2/\text{V}\cdot\text{s}$  at 300 K and  $501 \, \text{cm}^2/\text{V}\cdot\text{s}$  at 77 K were achieved after ATO encapsulation that are among the highest mobility values reported on ML  $\text{MoS}_2$ . We also analyzed the doping effect of ATO films on ML  $\text{MoS}_2$ , a phenomenon that is absent when stoichiometric  $\text{TiO}_2$  is used, using ab initio density functional theory (DFT) calculations that shows excellent agreement with our experimental findings. On the basis of the interfacial-oxygen-vacancy mediated doping as seen in the case of high- $\kappa$  ATO–ML  $\text{MoS}_2$ , we propose a mechanism for the mobility enhancement effect observed in TMD-based devices after encapsulation in a high- $\kappa$  dielectric environment.

**KEYWORDS:** Molybdenum disulfide ( $\text{MoS}_2$ ), field effect transistor, Schottky barrier, contact resistance, high- $\kappa$  dielectric, amorphous titanium suboxide (ATO), doping, intrinsic mobility



Research on two-dimensional (2D) layered materials has been on the rise ever since the isolation of graphene in 2004.<sup>1</sup> Despite its remarkable electrical, optical, and mechanical properties, the lack of a sizable band gap hinders the use of graphene in next generation digital electronic applications.<sup>2</sup> Alternatively, semiconducting layered transition metal dichalcogenides (TMDs) can circumvent this issue owing to their band-gaps, thereby paving the way for the realization of digital logic circuits utilizing 2D layered materials. Semiconducting TMDs offer unique advantages when incorporated into field effect transistors (FETs) in their atomically thin form. Their high transparency, mechanical flexibility, and mobility values higher than organic, amorphous, or polycrystalline semiconductors make them ideal candidates for use in future transparent and flexible electronics.<sup>3</sup> Moreover, their ultrathin body allows for excellent electrostatic gate control of the channel even at aggressively scaled channel lengths, thereby making them less susceptible to detrimental short channel effects.<sup>2–5</sup> Molybdenum disulfide ( $\text{MoS}_2$ ) has emerged as the

most popular and extensively studied semiconducting TMD over the past few years due to its natural abundance and excellent environmental stability. The potential of  $\text{MoS}_2$  has been demonstrated in various electronic and optoelectronic device applications including FETs,<sup>6</sup> photovoltaics,<sup>7</sup> photo-detectors,<sup>8</sup> sensors,<sup>9</sup> as well as in more complicated logic circuits such as inverters,<sup>10</sup> memory cells,<sup>11</sup> ring oscillators,<sup>12</sup> and so forth. However, FETs made from  $\text{MoS}_2$  and other TMDs suffer from a large contact resistance ( $R_C$ ) due to the Schottky barriers formed at the metal–TMD interface.<sup>13,14</sup> Moreover, extrinsic mobility limiting factors such as charged impurity scattering adversely affect the device performance.<sup>15</sup> Realization of ohmic contacts and minimization of mobility limiting factors is necessary to harvest the potential of  $\text{MoS}_2$  in

Received: January 26, 2015

Revised: June 12, 2015



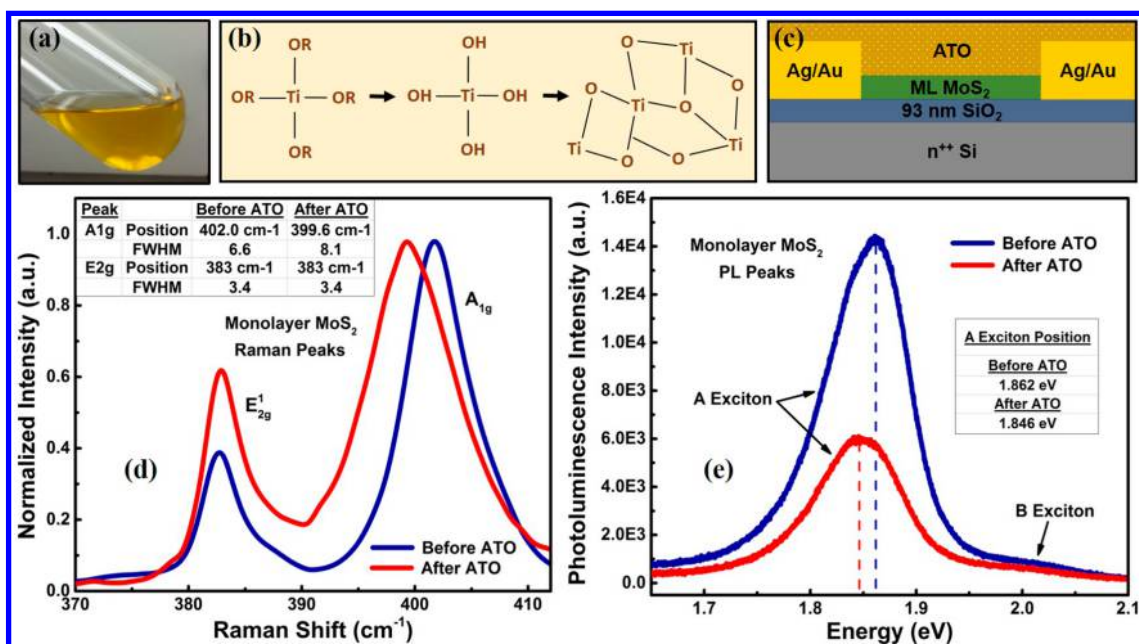


**Figure 1.** (a) Optical image of the as-prepared ATO precursor solution showing its characteristic yellowish orange color. (b) Schematic of chemical steps involved in the formation of ATO from its precursor molecules, namely titanium isopropoxide ( $R = CH(CH_3)_2$ ). (c) Schematic of a representative back-gated ML MoS<sub>2</sub> FET encapsulated by ATO. (d) Raman spectra of ML MoS<sub>2</sub> showing its characteristic A<sub>1g</sub> and E<sub>2g</sub> peaks before (blue) and after (red) ATO encapsulation illustrating the electron doping-induced changes. (e) Photoluminescence spectra of ML MoS<sub>2</sub> before (blue) and after (red) ATO encapsulation showing a redshift in the peak position of the A exciton.

future nanoelectronic applications, especially at aggressively scaled channel lengths.

In order to alleviate the large  $R_C$  in MoS<sub>2</sub> FETs, insightful work has been done by several groups over the past few years. Das et al. demonstrated the use of low work function scandium as an efficient electron injector into the conduction band of MoS<sub>2</sub>.<sup>16</sup> N-type charge transfer dopants such as potassium ions (K)<sup>17</sup> and polyethylenimine (PEI)<sup>18</sup> have been utilized, although these doping reagents are unstable in ambient conditions. The use of graphene–metal heterocontacts<sup>19</sup> and air stable doping via benzyl viologen (BV)<sup>20</sup> were shown to be effective strategies, but the  $R_C$  values were still greater than 1 k $\Omega$ · $\mu$ m and only moderate channel mobilities were achieved. More recently, the use of phase engineered contacts<sup>21</sup> and chloride doping<sup>22,23</sup> were demonstrated on MoS<sub>2</sub> with promising results. However, the stability of the phase engineered contacts under high-performance device operation is still unknown.<sup>21</sup> Furthermore, the chloride doping mechanism is unclear and it is speculated that the doping occurs due to filling of the naturally occurring sulfur vacancies in MoS<sub>2</sub> by chlorine atoms.<sup>23</sup> Besides doping and the corresponding  $R_C$  reduction, considerable effort has also been put into dielectric engineering utilizing high dielectric constant (high- $\kappa$ ) materials to reduce the scattering of carriers in MoS<sub>2</sub> devices. Although several high- $\kappa$  dielectrics have been investigated, atomic layer deposition (ALD) of alumina and hafnia have been the most common choices.<sup>6,10,15,24–27</sup>

In this Letter, we demonstrate an air stable, self-encapsulating, n-type charge transfer doping technique on ML MoS<sub>2</sub> utilizing amorphous titanium suboxide (ATO) thin films. The ATO can be solution processed in the form of a sol–gel precursor and its application involves a simple spin-coating process, thereby making this approach extremely facile and easily scalable in contrast to the phase engineering or chloride doping schemes that require several hours of treatment with

their respective chemical reagents.<sup>21–23</sup> Utilizing this technique, we achieved a very low  $R_C$  of  $\sim 180 \Omega \cdot \mu\text{m}$  on ML MoS<sub>2</sub>, which compares favorably to the  $R_C$  values obtained on 2–3 layer MoS<sub>2</sub> with phase engineered contacts<sup>21</sup> and is  $\sim 2.5$  times lower than the  $R_C$  reported on chloride-doped multilayer MoS<sub>2</sub> FETs.<sup>23</sup> An ON-current as high as 240  $\mu\text{A}/\mu\text{m}$  was achieved for a 450 nm channel length ( $L$ ) back-gated FET with an oxide thickness ( $t_{\text{ox}}$ ) of 93 nm at a drain-to-source voltage ( $V_{\text{DS}}$ ) of 2 V and back-gate overdrive voltage ( $V_{\text{BG}} - V_T$ ) of 70 V. Field-effect mobilities ( $\mu_{\text{FE}}$ ) as high as 83  $\text{cm}^2/\text{V}\cdot\text{s}$  and intrinsic mobilities ( $\mu_{\text{int}}$ ) as high as 102  $\text{cm}^2/\text{V}\cdot\text{s}$  were achieved on ML MoS<sub>2</sub> devices at room temperature (RT) upon ATO encapsulation. Temperature-dependent measurements revealed enhanced intrinsic mobilities approaching 501  $\text{cm}^2/\text{V}\cdot\text{s}$  in ATO encapsulated ML MoS<sub>2</sub> at 77 K. Density functional theory (DFT) analysis was performed to gain further insight into the doping mechanism of ATO films on ML MoS<sub>2</sub>.

The mechanism of charge transfer doping is particularly attractive for ultrathin layered materials because it does not involve any substantial distortion of the 2D crystal lattice.<sup>20</sup> Several charge transfer doping techniques that were previously demonstrated on carbon-based nanomaterials were also successfully demonstrated on MoS<sub>2</sub>.<sup>17,18,20</sup> Similarly, we investigate the effects of high- $\kappa$  ATO thin films on MoS<sub>2</sub> that serve as an n-type charge transfer dopant. For the purpose of this experiment, only ML MoS<sub>2</sub> flakes were considered. Details on materials and device fabrication methods can be found in Supporting Information S1, while the characterization tools and techniques are described in Supporting Information S2. ATO thin films were deposited on MoS<sub>2</sub> FETs by spin-coating at 3000 rpm and subsequent baking of an ATO sol–gel precursor solution [see Supporting Information S3 for its preparation method] at 90 °C on a hot plate for 15 min to dry the residual solvent and convert the precursor solution into ATO through hydrolysis. ATO thin films obtained using this process were

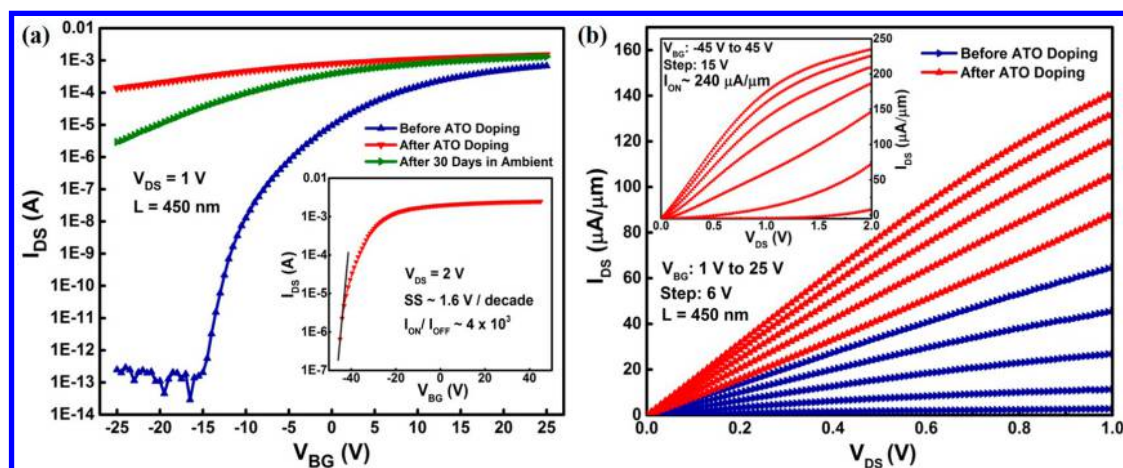


**Figure 2.** (a) Transfer characteristics, shown on a semilog scale, of a representative ML MoS<sub>2</sub> FET at  $V_{DS} = 1$  V before (blue) and after (red) ATO doping, and after 30 days of ambient exposure (green). Inset shows the transfer characteristics of the doped FET measured under larger gate ( $-45$  to  $45$  V) and drain biasing ( $2$  V) conditions. The channel length and width are  $450$  nm and  $10.4$   $\mu\text{m}$ , respectively. (b) Output characteristics of the same FET before (blue) and after (red) ATO doping. Inset shows the output characteristics under larger biasing conditions with the ON-current reaching up to  $240$   $\mu\text{A}/\mu\text{m}$  at a  $V_{BG}$  of  $45$  V and  $V_{DS}$  of  $2$  V.

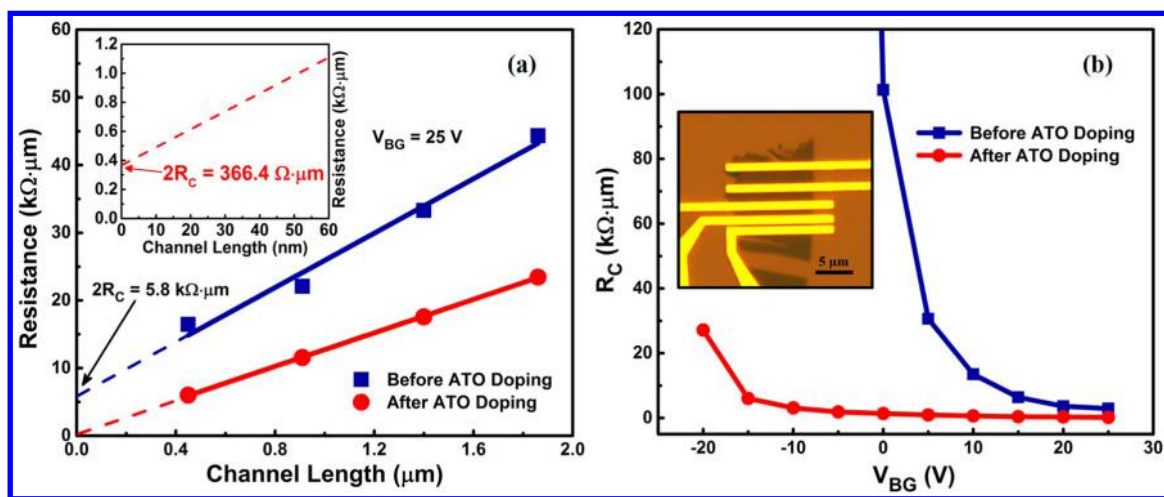
reported to have band-gaps of  $\sim 3.7^{28}$  and  $\sim 3.9$  eV<sup>29</sup> corresponding to a Ti:O ratio of  $1:1.34$ ,<sup>28</sup> and  $1:1.59$ ,<sup>29</sup> respectively. The amorphous nature of these films and their large band-gaps have been confirmed in literature by X-ray diffraction (XRD) and optical absorption measurements, respectively.<sup>28,29</sup> The Ti/O ratio in our films was estimated to be  $\sim 1:1.5$  from the XPS data [Supporting Information S4] confirming the oxygen deficiency. Also, from the reported band-gaps for ATO films with different Ti/O ratios,<sup>28,29</sup> the band gap of our films can be estimated to be between  $3.7$  and  $3.9$  eV. Therefore, ATO can effectively be regarded as a wide band gap amorphous oxide semiconductor. As TiO<sub>2</sub> can serve as channel for n-type thin film transistors,<sup>30–32</sup> it is important to first rule any parallel conduction paths that can be added to the MoS<sub>2</sub> channel by the encapsulating ATO layer. To test for possible conduction through the ATO film, a set of control devices without the MoS<sub>2</sub> channel were fabricated in exactly the same manner as the actual devices. No conduction was observed through the as-formed ATO layer even under higher biasing conditions (both back-gate and drain) than what was used in actual devices. Hence, the ATO films in our case were found to be completely insulating.

Figure 1a shows an image of the as-prepared ATO sol–gel precursor solution with a concentration of  $\sim 85$  mg/mL. Figure 1b shows a schematic of the chemistry responsible for the formation of ATO from titanium isopropoxide, its precursor molecules. A schematic of a back-gated FET encapsulated by ATO is illustrated in Figure 1c. The doping of MoS<sub>2</sub> leads to changes in its Raman and photoluminescence (PL) spectra. Figure 1d compares the normalized Raman spectra of an as-exfoliated ML MoS<sub>2</sub> flake (blue) to that of the same flake after encapsulation by ATO (red). The peak positions of the out-of-plane  $A_{1g}$  and in-plane  $E_{2g}^1$  peaks for the bare ML MoS<sub>2</sub> are at  $402.0$  and  $383.0$   $\text{cm}^{-1}$ , respectively, corresponding to a peak separation of  $19$   $\text{cm}^{-1}$ . This peak separation is characteristic of ML MoS<sub>2</sub>.<sup>33</sup> Upon encapsulation with ATO, the  $E_{2g}^1$  peak position and peak full-width half-maximum (fwhm) remain relatively unchanged. On the other hand, the  $A_{1g}$  peak shows a distinct broadening with its fwhm increasing from  $6.6$  to  $8.1$   $\text{cm}^{-1}$ , as well as a redshift from  $402.0$  to  $399.6$   $\text{cm}^{-1}$ . This redshift and peak broadening of the  $A_{1g}$  Raman mode are

characteristic of doped MoS<sub>2</sub> and have been observed in previous doping studies.<sup>20</sup> Figure 1e compares the PL spectra of a ML MoS<sub>2</sub> flake before (blue) and after (red) encapsulation with ATO. Before encapsulation, the peak position of the A exciton is at  $1.86$  eV, consistent with reported values for ML MoS<sub>2</sub>.<sup>34</sup> Upon ATO encapsulation, the A exciton peak shows a decrease in intensity and a redshift of  $16$  meV, which can be attributed to the formation of negatively charged trions from excitons as a result of the increased electron concentration.<sup>35,36</sup> The pronounced changes in the Raman and PL spectra of ML MoS<sub>2</sub> upon ATO encapsulation clearly indicate the n-type doping effects of ATO on MoS<sub>2</sub>.

The transfer characteristics of a representative back-gated MoS<sub>2</sub> FET at  $V_{DS} = 1$  V, before and after ATO encapsulation, as well as after one month of exposure to ambient conditions are shown in Figure 2a. All FETs were fabricated on  $93$  nm SiO<sub>2</sub>/n<sup>+</sup> Si substrates. The transfer curve before doping (blue) indicates a strong electrostatic gate control over the channel with a threshold voltage ( $V_T$ ) of  $7$  V, extracted from the linear region of the transfer characteristics, and an  $I_{ON}/I_{OFF}$  ratio up to  $10^8$ . Upon encapsulation with ATO, the gate modulation is significantly reduced (red curve), and the  $V_T$  shifts to  $-25$  V. This large negative  $V_T$  shift is indicative of the n-doping effect of ATO. The 2D sheet electron concentration ( $n_{2D}$ ) after ATO doping can be estimated as  $n_{2D} = (C_{OX} |\Delta V_T|)/q$ , where  $q$  is the electron charge,  $C_{OX} = 3.71 \times 10^{-8}$  F/cm<sup>2</sup> is the gate oxide capacitance, and  $\Delta V_T = -32$  V is the shift in threshold voltage right after doping. The extracted value of  $n_{2D}$  for this device upon doping was  $7.4 \times 10^{12}$  cm<sup>-2</sup>. Previous doping studies on MoS<sub>2</sub> utilizing K ions<sup>17</sup> and benzyl viologen<sup>20</sup> reported  $n_{2D}$  values of  $1 \times 10^{13}$  cm<sup>-2</sup> and  $1.2 \times 10^{13}$  cm<sup>-2</sup>, respectively. The  $n_{2D}$  value as a result of ATO doping is slightly lower in our case, however, it should be noted that our experiments used ML flakes unlike previous studies that utilized multilayer flakes. The long-term air stability of encapsulated ATO doping is evident from the electrical data as even after 30 days of exposure to ambient conditions, the device shows similar ON-currents, a weak gate modulation, and has an  $n_{2D} = 3.7 \times 10^{12}$  cm<sup>-2</sup> (green curve). Moreover, by virtue of being self-encapsulating, ATO films protect the underlying MoS<sub>2</sub> channel from the degrading effects of atmospheric adsorbates. However, there is slight





**Figure 3.** (a) Plot of total resistance as a function of channel length as determined from the TLM structure before (blue) and after (red) ATO doping at a  $V_{BG}$  of 25 V. The solid blue and red lines are linear fits to the data. The  $R_C$  and  $L_T$  extracted before doping are  $2.9 k\Omega \cdot \mu m$  and 145 nm, respectively. After ATO doping, the extracted  $R_C$  is  $\sim 180 \Omega \cdot \mu m$  and  $L_T$  is 15 nm. Inset: zoomed in view of the extrapolated dashed red line. (b) Extracted  $R_C$  as a function of  $V_{BG}$  before (blue) and after (red) ATO doping. The  $R_C$  shows a strong gate dependence before doping and a weak gate dependence after doping. Inset: optical micrograph image of the as-fabricated TLM structure.

performance degradation after extended ambient exposure in ATO encapsulated devices [Supporting Information S5].

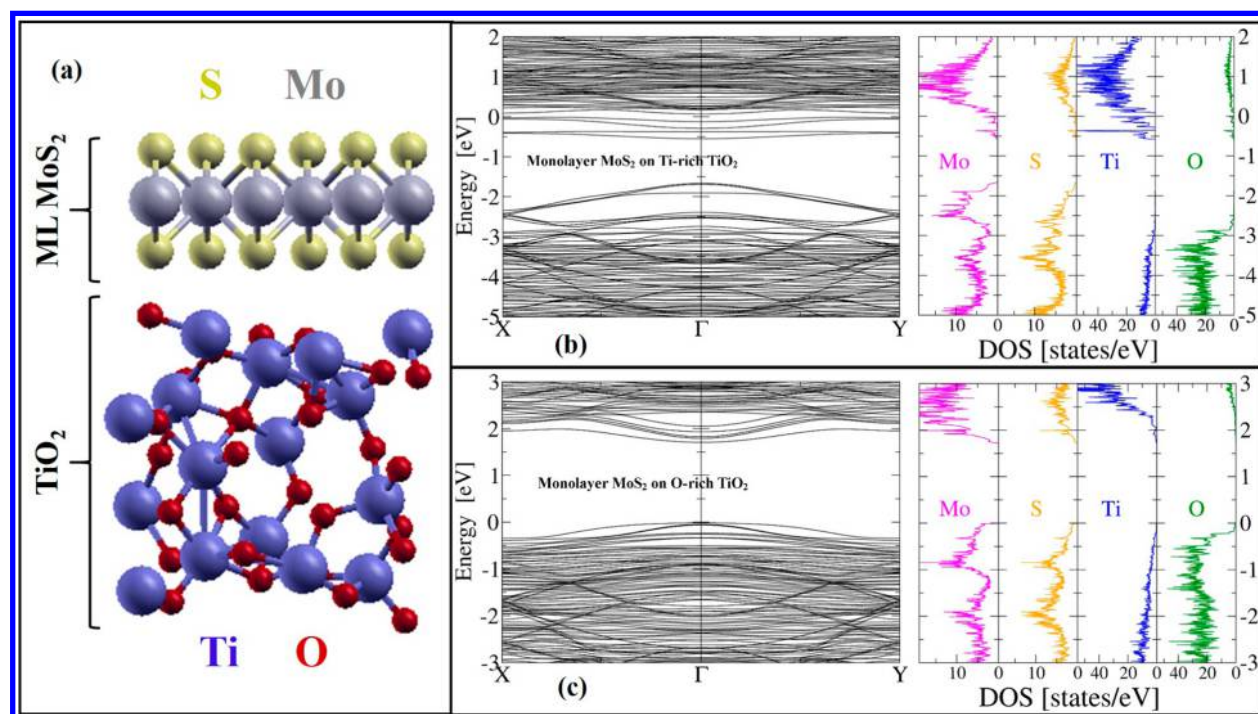
The inset of Figure 2a shows the transfer characteristics of the same device at larger gate and drain biases following the ATO encapsulation. The 450 nm channel length device could be switched off to a moderate extent ( $I_{ON}/I_{OFF} = 4 \times 10^3$ , subthreshold swing = 1.6 V/decade) at large negative gate biases even though  $V_{DS}$  was as high as 2 V. Further optimization and control over the starting concentrations of the ATO precursor solution or realization of top gated devices with ATO encapsulated S-D access regions would help yield an ideal balance between  $I_{ON}/I_{OFF}$  ratio and high saturation ON-currents. Figure 2b shows the output characteristics of the same device as in Figure 2a. After ATO encapsulation, the ON current of the ML device at  $V_{DS} = 1$  V and  $V_{BG} = 25$  V is 144  $\mu A/\mu m$ , which is 2.5 times greater than the corresponding value for the undoped device. The inset of Figure 2b shows the output characteristics of the same device subject to larger biasing conditions. At a  $V_{DS}$  of 2 V and  $V_{BG}$  of 45 V, the ON current is as high as 240  $\mu A/\mu m$  showing the onset of current saturation at large positive gate and drain biases. Our ATO-doped ML  $MoS_2$  FET with an ON current of 240  $\mu A/\mu m$  compares well with the highest drain current to date on chloride-doped multilayer  $MoS_2$  FETs,<sup>22,23</sup> taking into account the fact that the channel length in our case was 4.5 times larger and the device was made on a ML flake.

In order to quantify the effect of ATO doping on the electrical contact between the metal (Ag) and the ML  $MoS_2$ , a transfer length method (TLM) analysis was carried out. A suitable large area ML flake was identified, upon which a set of contacts were fabricated with different channel lengths as shown in the inset of Figure 3b. The basic equation underlying the TLM analysis can be written as  $R_{TOTAL} = (R_{SH}L)/W + 2R_C$ , where  $R_{TOTAL}$  is the total measured resistance of a channel between two contacts,  $R_{SH}$  is the sheet resistance of the channel,  $L$  and  $W$  are the channel's length and width, respectively, and  $R_C$  is the contact resistance. By fitting a plot of  $(R_{TOTAL} \cdot W)$  as a function of  $L$ , key parameters such as  $R_{SH}$ ,  $R_C$ , and transfer length ( $L_T$ ) can be extracted. Figure 3a shows the total resistance, measured at a  $V_{BG}$  of 25 V and  $V_{DS}$  of 0.1 V,

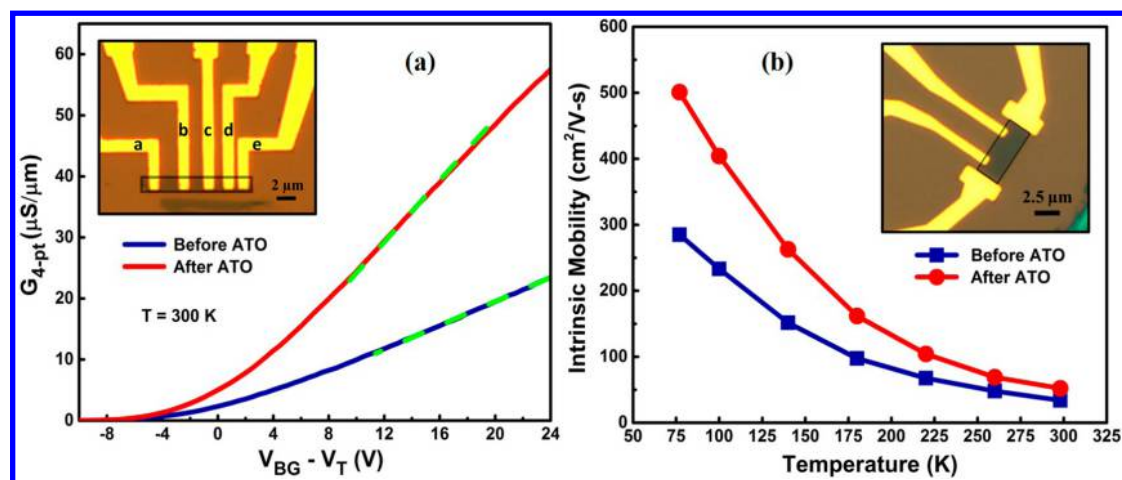
as a function of  $L$  before (blue) and after (red) ATO encapsulation. From a linear fit to the measured resistances before doping, an  $R_{SH}$  of 20.1  $k\Omega/\square$ ,  $R_C$  of  $2.9 k\Omega \cdot \mu m$  and a transfer length ( $L_T$ ) of 145 nm were extracted. Fitting the measured resistances after ATO encapsulation, we extracted an  $R_{SH}$  of 12.4  $k\Omega/\square$ ,  $R_C$  of  $\sim 180 \Omega \cdot \mu m$  (inset of Figure 3a), and an  $L_T$  of 15 nm. This significant reduction in  $R_{SH}$ ,  $R_C$ , and  $L_T$  upon ATO encapsulation reflects the efficacy of this doping technique. This is the lowest reported  $R_C$  value among all previous n-type doping studies on  $MoS_2$ <sup>17,18,20</sup> and compares well with the recently reported record low  $R_C$  value ( $\sim 80 \Omega \cdot \mu m$  at a  $V_{BG}$  of 30 V) on  $MoS_2$  with phase engineered contacts.<sup>21</sup>

Figure 3b shows the extracted  $R_C$  values plotted as a function of  $V_{BG}$  before and after ATO encapsulation. For the undoped case (blue curve), the  $R_C$  shows a strong dependence on gate bias and increases exponentially at negative gate biases due to the large Schottky barriers present at the contacts. On the other hand, for the ATO doped case (red curve), the  $R_C$  is fairly independent of the applied gate bias for  $V_{BG} > -10$  V. This results from the substantial thinning of the Schottky barrier width as a consequence of heavy doping at the contact regions. This Schottky barrier thinning effect is also apparent in the transfer characteristics temperature dependence, and in the output characteristics measured at 77 K of a back-gated ML  $MoS_2$  FET after ATO doping [Supporting Information S6]. Thus, in the ATO-doped ML  $MoS_2$  devices the effective Schottky barriers are significantly reduced even though the doping occurs along the contact edges as opposed to directly underneath the contacts. We note that this ATO doping effect on ML  $MoS_2$  is absent when stoichiometric  $TiO_2$  is used, as demonstrated previously in the case of graphene.<sup>29,37</sup> This was verified by depositing  $TiO_2$  on back-gated ML  $MoS_2$  FETs utilizing a recently demonstrated technique<sup>38</sup> [Supporting Information S7].

To gain further insight into the doping mechanism of  $MoS_2$  by ATO, an ab initio DFT analysis was carried out to study the effects of both a Ti-rich and an O-rich interface of an underlying  $TiO_2$  slab on the electronic structure of ML  $MoS_2$  via band-structure and atom-projected density-of-states (AP-DOS) calculations. The DFT simulation was performed using



**Figure 4.** (a) Supercell showing the composite crystal structure consisting of ML MoS<sub>2</sub> on an underlying rutile-TiO<sub>2</sub> slab as simulated in VASP. For simulating the O-rich TiO<sub>2</sub> case, the TiO<sub>2</sub> slab was left unaltered. In contrast, for the Ti-rich TiO<sub>2</sub> case, a suitable number of O vacancies were created in TiO<sub>2</sub> at the ML MoS<sub>2</sub>-TiO<sub>2</sub> interface so as to mimic the MoS<sub>2</sub>-ATO scenario. (b) Band-structure and atom-projected-density-of-states (AP-DOS) plots for the ML MoS<sub>2</sub>-Ti-rich TiO<sub>2</sub> case. From the plots, it can be deduced that in the presence of O vacancies, electronic states from Ti atoms are introduced near the conduction band edge of ML MoS<sub>2</sub> causing the Fermi level to get pinned above the conduction band indicating strong doping. (c) Band-structure and AP-DOS plots for the ML MoS<sub>2</sub>-O-rich TiO<sub>2</sub> case. No doping effect is seen in this case and the Fermi level remains pinned at the valence band edge. (Simulations were done assuming 0 K).



**Figure 5.** (a) Four-point conductance ( $G_{4-pt}$ ) curves as a function of the gate overdrive ( $V_{BG} - V_T$ ), measured between contacts a, b, c, and d of the device shown in the inset, before (blue) and after (red) ATO encapsulation at RT. Dashed light green lines represent the regions from where the maximum slope was extracted for the calculation of intrinsic mobility of the ML MoS<sub>2</sub> flake before/after ATO encapsulation. The length and width of the active region are 1.45 and 1.42  $\mu m$ , respectively. Contacts d and e (separated by 460 nm) were used to extract the two-point field effect mobility before/after ATO encapsulation. (b) Intrinsic mobility of ML MoS<sub>2</sub> as a function of temperature before (blue) and after (red) ATO encapsulation. Optical micrograph of the four-point device is shown in the inset. The length and width of the active region are 2.3 and 2.5  $\mu m$ , respectively. The intrinsic mobilities are enhanced after ATO encapsulation reaching up to 501  $cm^2/V-s$  at 77 K. (ML MoS<sub>2</sub> flakes are outlined at their edges.)

the Vienna ab initio simulation package (VASP)<sup>39,40</sup> and exact details of the methodology employed here are described elsewhere.<sup>41</sup> Briefly, our simulations were performed by constructing a supercell of ML MoS<sub>2</sub> on an approximately 1 nm thick TiO<sub>2</sub> slab. Atomic relaxation was performed within a rectangular supercell ( $a = 9.366$  Å,  $b = 5.407$  Å) chosen to

reduce the lattice mismatch between ML MoS<sub>2</sub> and rutile-TiO<sub>2</sub> as shown in Figure 4a. The rutile phase was chosen for the simulation because it is the most common natural form of TiO<sub>2</sub>.<sup>42</sup> As stated before, we consider two possible terminations for the TiO<sub>2</sub> slab, a Ti-rich TiO<sub>2</sub> slab and an O-rich TiO<sub>2</sub> slab. For the Ti-rich TiO<sub>2</sub> case, the surface O atoms were removed

from the supercell corresponding to an O-vacancy density of  $7.896 \times 10^{14}/\text{cm}^2$  in order to mimic the ATO structure with interfacial O-vacancies. In these 0 K simulations, the highest occupied state corresponds to the 0 eV reference energy. Figure 4b shows the band structure of ML MoS<sub>2</sub> on a Ti-rich TiO<sub>2</sub> slab depicting occupied conduction bands below the Fermi level leading to a system that appears metallic. From the corresponding AP-DOS plot shown at the right, we can observe that the occupied conduction bands can be attributed to Ti, Mo, and S atom states implying that the additional states introduced by the Ti atoms appear near the conduction band states of ML MoS<sub>2</sub>. For the composite MoS<sub>2</sub>–TiO<sub>2</sub> system, this phenomenon can be interpreted as a transfer of electrons into the lower conduction-band-edge of the ML MoS<sub>2</sub> layer analogous to modulation doping. In contrast, this phenomenon is absent in the case of ML MoS<sub>2</sub> on the O-rich TiO<sub>2</sub> slab, as depicted in Figure 4c, wherein we have an ideal TiO<sub>2</sub> surface without any O-vacancies in the supercell. Here, the Fermi level is pinned at the valence band edge and the conduction band states remain unoccupied. Hence, our theoretical findings are in excellent agreement with our experimental results. It is to be noted that in the band-structures depicted in Figure 4b,c, the conduction band minima and the valence band maxima are located at the  $\Gamma$  point as opposed to the K point for ML MoS<sub>2</sub>. This is because using a bigger supercell in the DFT simulations results in the corresponding Brillouin zone being smaller and hence the K point folds into the  $\Gamma$  point.<sup>41</sup>

An added advantage of using high- $\kappa$  ATO as a self-encapsulating dopant is the intrinsic mobility enhancement of ML MoS<sub>2</sub> as extracted from four-point back-gated devices that exclude contact resistance effects. High- $\kappa$  dielectric engineering, using ALD deposited hafnia and alumina, has been used widely on MoS<sub>2</sub> and other TMDs.<sup>6,10,16,24,25,43</sup> Although the exact mechanism is still unclear, it is believed that the presence of a high- $\kappa$  environment enhances the carrier mobility by “screening” the Coulomb interactions with charged impurities, as well as by quenching the homopolar phonon modes of MoS<sub>2</sub>.<sup>15,44,45</sup> Although ATO films have been shown to have a  $\kappa$ -value ranging between 70–120,<sup>46</sup> the  $\kappa$ -value of our solution-processed ATO films was extracted to be  $\sim 10$  from capacitance–voltage measurements, a value comparable to the  $\kappa$ -values reported for alumina and hafnia.<sup>47</sup> Figure 5a shows the measured four-point conductance ( $G_{4\text{-pt}}$ ) as a function of  $V_{\text{BG}} - V_{\text{T}}$  for a ML MoS<sub>2</sub> device (shown in the inset with the flake outlined at its edges) before and after ATO encapsulation. The four left-most contacts of the device (a, b, c, and d) were used for the four point measurement that was done at RT. Current was passed between the outer two contacts (a, d) while the inner two contacts (b, c) served as the voltage probes. A marked difference exists between the slopes of the curves from the bare device (blue) and after its encapsulation in ATO (red). Intrinsic mobility ( $\mu_{\text{int}}$ ) was calculated using the expression  $\mu_{\text{int}} = (L/W) (1/C_{\text{OX}}) (dG_{4\text{-pt}}/dV_{\text{BG}}|_{\text{max}})$  where  $L = 1.45 \mu\text{m}$  and  $W = 1.42 \mu\text{m}$  are the length and width of the active region bounded by contacts b and c, respectively,  $C_{\text{OX}}$  is the geometric oxide capacitance, and  $(dG_{4\text{-pt}}/dV_{\text{BG}}|_{\text{max}})$  is the maximum slope of the four point conductance curves as marked by dashed light-green lines in the figure. For the bare ML MoS<sub>2</sub>, we extracted a  $\mu_{\text{int}}$  of 48 cm<sup>2</sup>/V-s at RT, whereas after encapsulation  $\mu_{\text{int}}$  increased to 102 cm<sup>2</sup>/V-s ( $\sim 2\times$  improvement). This value is among the highest intrinsic mobilities reported for ML MoS<sub>2</sub> at RT and comes close to the calculated RT phonon-limited mobility of 130 cm<sup>2</sup>/V-s, a more realistic

estimation in which the effect of intervalley scattering between the K and Q valleys, separated from each other in energy by just 70 meV, was also considered.<sup>48</sup> Though this was the best RT intrinsic mobility enhancement we observed upon ATO encapsulation ( $>2\times$  improvement), the effect itself was observed in five other four-point devices. The two-point  $\mu_{\text{FE}}$  measured between contacts “d” and “e” ( $L = 0.46 \mu\text{m}$ ,  $W = 1.42 \mu\text{m}$ ) at a  $V_{\text{DS}}$  of 100 mV before and after encapsulation was 24 cm<sup>2</sup>/V-s and 83 cm<sup>2</sup>/V-s, respectively, showing a  $> 3\times$  improvement [Supporting Information S8]. Comparing the two point  $\mu_{\text{FE}}$  of this device with the four-point  $\mu_{\text{int}}$  of the parent MoS<sub>2</sub> flake, we see that the ratio  $\mu_{\text{int}}/\mu_{\text{FE}}$  decreases from 2.02 before ATO encapsulation to 1.23 after ATO encapsulation implying that the two-point  $\mu_{\text{FE}}$  of this device approaches the four-point  $\mu_{\text{int}}$  of the parent flake due to the doping by ATO.

Figure 5b shows the maximum four-point intrinsic mobility of another ML MoS<sub>2</sub> device (shown in the inset) as a function of temperature. The length and width of the active region are 2.3 and 2.5  $\mu\text{m}$  (flake width), respectively. Before ATO encapsulation (blue), the intrinsic mobility varies from 30 cm<sup>2</sup>/V-s at RT to 285 cm<sup>2</sup>/V-s at 77 K. After ATO encapsulation (red), the values range from 52 cm<sup>2</sup>/V-s at RT to 501 cm<sup>2</sup>/V-s at 77 K following a similar trend. This value of 501 cm<sup>2</sup>/V-s in ATO-encapsulated MoS<sub>2</sub> is among the highest intrinsic mobilities reported to date on ML MoS<sub>2</sub> at 77 K and compares well with the recent work on ultrahigh mobility MoS<sub>2</sub> that is encapsulated in hexagonal boron nitride and contacted by graphene.<sup>49</sup> Although this mobility enhancement may be attributed to the high- $\kappa$  nature of the encapsulating ATO, we know that the  $n_{2\text{D}}$  in the MoS<sub>2</sub> channel is increased as the high- $\kappa$  ATO film dopes the MoS<sub>2</sub> owing to its interfacial oxygen vacancies. Increased carrier densities in a nondegenerate 2D channel aids in enhancing the carrier mobility by screening the charged impurities, as has been demonstrated both theoretically<sup>44</sup> and experimentally<sup>50</sup> in ML MoS<sub>2</sub>. Furthermore, the increased electron concentration also serves to soften the homopolar phonons of MoS<sub>2</sub> as evident from the red shift and broadening of the out-of-plane A<sub>1g</sub> Raman mode of ML MoS<sub>2</sub> upon ATO encapsulation. Our results, therefore, give important insight into the mechanism of mobility enhancement in MoS<sub>2</sub> devices effected by high- $\kappa$  dielectrics. In light of our ATO–MoS<sub>2</sub> results, it is plausible that this doping effect can be caused by other high- $\kappa$  dielectrics, such as ALD-deposited alumina or hafnia, if they have inherent oxygen vacancies at their interfaces with MoS<sub>2</sub>. Given the amorphous nature of the ALD grown high- $\kappa$  dielectrics, it is highly possible that oxygen vacancies exist in their structure. In fact, our recent investigation<sup>41</sup> reveals that interfacial oxygen vacancies in alumina or hafnia lead to the creation of donor states near the conduction band of MoS<sub>2</sub>. These donor states originate from the uncompensated aluminum and hafnium atoms at the high- $\kappa$ –MoS<sub>2</sub> interface, much akin to our case of uncompensated titanium atoms at the ATO–MoS<sub>2</sub> interface, resulting in n-type doping of the ML MoS<sub>2</sub> channel. On the other hand, when the alumina or hafnia is perfectly stoichiometric, no doping effect is observed. Therefore, we propose that this interfacial-oxygen-vacancy-mediated doping effect plays a prominent role in enhancing both the intrinsic and field-effect mobility in high- $\kappa$  encapsulated TMD devices. Upon high- $\kappa$  encapsulation, there would be an increase in the  $n_{2\text{D}}$  of the TMD channel even before the application of external gate or drain biases, and this increased  $n_{2\text{D}}$  would screen out the charged impurities, suppress



the homopolar phonons, and reduce the effective Schottky barrier at the contacts to a greater extent than in bare devices. Hence, when the external biases are applied, the electrons would be injected more easily and will move across the channel with less scattering, resulting in higher transconductance at relatively lower gate and drain biases in high- $\kappa$  encapsulated TMD FETs.

To conclude, we have demonstrated that high- $\kappa$  ATO films can be used as an n-type charge transfer dopant on ML MoS<sub>2</sub>. The fact that ATO encapsulated ML MoS<sub>2</sub> devices exhibited comparable or better performance than previous doping and high- $\kappa$  studies bears testimony to the superior doping and mobility enhancing capabilities of ATO thin films. Moreover, high- $\kappa$  ATO can be deposited by a simple spin coating process that makes this doping approach attractive when compared to other time-consuming doping techniques. Utilizing this technique on ML MoS<sub>2</sub>, we demonstrated two-point field effect mobility as high as 83 cm<sup>2</sup>/V-s at RT, four-point intrinsic mobility as high as 102 cm<sup>2</sup>/V-s at RT and 501 cm<sup>2</sup>/V-s at 77 K. ON-currents as high as 240  $\mu$ A/ $\mu$ m for a 450 nm channel length device, and a record low  $R_C$  of 180  $\Omega$ - $\mu$ m were demonstrated on ML MoS<sub>2</sub> after ATO encapsulation. In addition, we also shed light on the interfacial-oxygen-vacancy mediated doping of MoS<sub>2</sub> by high- $\kappa$  dielectrics, in general, leading to improved screening of charged impurities, suppression of homopolar phonon scattering, and reduction of the effective Schottky barriers at the contacts. Future work includes studying the stoichiometry and thickness scalability of ATO films and their effect on the performance and air stability of TMD-based devices.

## ■ ASSOCIATED CONTENT

### ● Supporting Information

Description of materials and device fabrication methods, characterization tools and techniques, preparation of the ATO sol-gel precursor solution, XPS analysis of the as-deposited ATO films, performance degradation in ATO encapsulated devices and possible remedies, transfer characteristics temperature dependence and output characteristics at 77 K of a back-gated ML MoS<sub>2</sub> FET before/after ATO doping, deposition method of TiO<sub>2</sub> and its effect on ML MoS<sub>2</sub> FET performance, and transfer curves used for the mobility extraction of the two-point device in Figure 5a. The Supporting Information is available free of charge on the ACS Publications website at DOI: 10.1021/acs.nanolett.5b00314.

## ■ AUTHOR INFORMATION

### Corresponding Author

\*E-mail: amritesh557@utexas.edu.

### Notes

The authors declare no competing financial interest.

## ■ ACKNOWLEDGMENTS

This work was supported by the NRI SWAN center, NSF NNIN, and Intel. The authors would like to thank the Army Research Office (ARO) for partial support of this work under STTR award number W911NF-14-P-0030.

## ■ REFERENCES

- (1) Novoselov, K. S.; Geim, A. K.; Morozov, S. V.; Jiang, D.; Zhang, Y.; Dubonos, S. V.; Grigorieva, I. V.; Firsov, A. A. *Science* **2004**, *306*, 666–669.
- (2) Wang, Q. H.; Kalantar-Zadeh, K.; Kis, A.; Coleman, J. N.; Strano, M. S. *Nat. Nanotechnol.* **2012**, *7*, 699–712.
- (3) Jariwala, D.; Sangwan, V. K.; Lauhon, L. J.; Marks, T. J.; Hersam, M. C. *ACS Nano* **2014**, *8*, 1102–1120.
- (4) Liu, H.; Neal, A. T.; Ye, P. D. *ACS Nano* **2012**, *6*, 8563–8569.
- (5) Das, S.; Appenzeller, J. In *2013 71st Annual Device Research Conference (DRC)*, Notre Dame, IN, June 23–26, 2013; IEEE, pp 153–154.
- (6) Radisavljevic, B.; Radenovic, A.; Brivio, J.; Giacometti, V.; Kis, A. *Nat. Nanotechnol.* **2011**, *6*, 147–150.
- (7) Fontana, M.; Deppe, T.; Boyd, A. K.; Rinzan, M.; Liu, A. Y.; Paranjape, M.; Barbara, P. *Sci. Rep.* **2013**, *3*, 1634.
- (8) Lopez-Sanchez, O.; Lembke, D.; Kayci, M.; Radenovic, A.; Kis, A. *Nat. Nanotechnol.* **2013**, *8*, 497–501.
- (9) Late, D. J.; Huang, Y.-K.; Liu, B.; Acharya, J.; Shirodkar, S. N.; Luo, J.; Yan, A.; Charles, D.; Waghmare, U. V.; Dravid, V. P.; Rao, C. N. R. *ACS Nano* **2013**, *7*, 4879–4891.
- (10) Radisavljevic, B.; Whitwick, M. B.; Kis, A. *ACS Nano* **2011**, *5*, 9934–9938.
- (11) Bertolazzi, S.; Krasnozhan, D.; Kis, A. *ACS Nano* **2013**, *7*, 3246–3252.
- (12) Wang, H.; Yu, L.; Lee, Y.-H.; Shi, Y.; Hsu, A.; Chin, M. L.; Li, L.-J.; Dubey, M.; Kong, J.; Palacios, T. *Nano Lett.* **2012**, *12*, 4674–4680.
- (13) Yoon, Y.; Ganapathi, K.; Salahuddin, S. *Nano Lett.* **2011**, *11*, 3768–3773.
- (14) Gong, C.; Colombo, L.; Wallace, R. M.; Cho, K. *Nano Lett.* **2014**, *14*, 1714–1720.
- (15) Radisavljevic, B.; Kis, A. *Nat. Mater.* **2013**, *12*, 815–820.
- (16) Das, S.; Chen, H.-Y.; Penumatcha, A. V.; Appenzeller, J. *Nano Lett.* **2012**, *13*, 100–105.
- (17) Fang, H.; Tosun, M.; Seol, G.; Chang, T. C.; Takei, K.; Guo, J.; Javey, A. *Nano Lett.* **2013**, *13*, 1991–1995.
- (18) Du, Y.; Liu, H.; Neal, A. T.; Si, M.; Ye, P. D. *IEEE Electron Device Lett.* **2013**, *34*, 1328–1330.
- (19) Du, Y.; Yang, L.; Zhang, J.; Liu, H.; Majumdar, K.; Kirsch, P. D.; Ye, P. D. *IEEE Electron Device Lett.* **2014**, *35*, 599–601.
- (20) Kiriya, D.; Tosun, M.; Zhao, P.; Kang, J. S.; Javey, A. *J. Am. Chem. Soc.* **2014**, *136*, 7853–7856.
- (21) Kappera, R.; Voiry, D.; Yalcin, S. E.; Branch, B.; Gupta, G.; Mohite, A. D.; Chhowalla, M. *Nat. Mater.* **2014**, *13*, 1128–1134.
- (22) Yang, L.; Majumdar, K.; Liu, H.; Du, Y.; Wu, H.; Hatzistergos, M.; Hung, P. Y.; Tieckelmann, R.; Tsai, W.; Hobbs, C.; Ye, P. D. *Nano Lett.* **2014**, *14*, 6275–6280.
- (23) Yang, L.; Majumdar, K.; Du, Y.; Liu, H.; Wu, H.; Hatzistergos, M.; Hung, P. Y.; Tieckelmann, R.; Tsai, W.; Hobbs, C.; Ye, P. D. In *2014 Symposium on VLSI Technology (VLSI-Technology): Digest of Technical Papers*, Honolulu, HI, June 9–12, 2014; IEEE, pp 1–2.
- (24) Chang, H.-Y.; Yang, S.; Lee, J.; Tao, L.; Hwang, W.-S.; Jena, D.; Lu, N.; Akinwande, D. *ACS Nano* **2013**, *7*, 5446–5452.
- (25) Liu, H.; Ye, P. D. *IEEE Electron Device Lett.* **2012**, *33*, 546–548.
- (26) Kim, S.; Konar, A.; Hwang, W.-S.; Lee, J. H.; Lee, J.; Yang, J.; Jung, C.; Kim, H.; Yoo, J.-B.; Choi, J.-Y.; Jin, Y. W.; Lee, S. Y.; Jena, D.; Choi, W.; Kim, K. *Nat. Commun.* **2012**, *3*, 1011.
- (27) McDonnell, S.; Brennan, B.; Azcatl, A.; Lu, N.; Dong, H.; Buie, C.; Kim, J.; Hinkle, C. L.; Kim, M. J.; Wallace, R. M. *ACS Nano* **2013**, *7*, 10354–10361.
- (28) Kim, J. Y.; Kim, S. H.; Lee, H.-H.; Lee, K.; Ma, W.; Gong, X.; Heeger, A. J. *Adv. Mater.* **2006**, *18*, 572–576.
- (29) Ho, P.-H.; Yeh, Y.-C.; Wang, D.-Y.; Li, S.-S.; Chen, H.-A.; Chung, Y.-H.; Lin, C.-C.; Wang, W.-H.; Chen, C.-W. *ACS Nano* **2012**, *6*, 6215–6221.
- (30) Zhong, N.; Cao, J. J.; Shima, H.; Akinaga, H. *IEEE Electron Device Lett.* **2012**, *33*, 1009–1011.
- (31) Shih, W. S.; Young, S. J.; Ji, L. W.; Water, W.; Shiu, H. W. *J. Electrochem. Soc.* **2011**, *158*, H609–H611.
- (32) Wobkenberg, P. H.; Ishwara, T.; Nelson, J.; Bradley, D. D. C.; Haque, S. A.; Anthopoulos, T. D. *Appl. Phys. Lett.* **2010**, *96*, 082116–082116–3.



- (33) Li, H.; Zhang, Q.; Yap, C. C. R.; Tay, B. K.; Edwin, T. H. T.; Olivier, A.; Baillargeat, D. *Adv. Funct. Mater.* **2012**, *22*, 1385–1390.
- (34) Splendiani, A.; Sun, L.; Zhang, Y.; Li, T.; Kim, J.; Chim, C.-Y.; Galli, G.; Wang, F. *Nano Lett.* **2010**, *10*, 1271–1275.
- (35) Mak, K. F.; He, K.; Lee, C.; Lee, G. H.; Hone, J.; Heinz, T. F.; Shan, J. *Nat. Mater.* **2013**, *12*, 207–211.
- (36) Mouri, S.; Miyauchi, Y.; Matsuda, K. *Nano Lett.* **2013**, *13*, 5944–5948.
- (37) McCreary, K. M.; Pi, K.; Kawakami, R. K. *Appl. Phys. Lett.* **2011**, *98*, 192101–192101–3.
- (38) Corbet, C. M.; McClellan, C.; Kim, K.; Sonde, S.; Tutuc, E.; Banerjee, S. K. *ACS Nano* **2014**, *8*, 10480–10485.
- (39) Kresse, G.; Furthmüller, J. *Comput. Mater. Sci.* **1996**, *6*, 15–50.
- (40) Kresse, G.; Furthmüller, J. *Phys. Rev. B* **1996**, *54*, 11169–11186.
- (41) Valsaraj, A.; Chang, J.; Rai, A.; Register, L. F.; Banerjee, S. K. *2D Materials*, submitted for publication, **2015**.
- (42) Muscat, J.; Swamy, V.; Harrison, N. M. *Phys. Rev. B* **2002**, *65*, 224112.
- (43) Liu, W.; Kang, J.; Sarkar, D.; Khatami, Y.; Jena, D.; Banerjee, K. *Nano Lett.* **2013**, *13*, 1983–1990.
- (44) Ong, Z.-Y.; Fischetti, M. V. *Phys. Rev. B* **2013**, *88*, 165316.
- (45) Kaasbjerg, K.; Thygesen, K. S.; Jacobsen, K. W. *Phys. Rev. B* **2012**, *85*, 115317.
- (46) Dover, R. B. van. *Appl. Phys. Lett.* **1999**, *74*, 3041–3043.
- (47) Robertson, J. *Eur. Phys. J. - Appl. Phys.* **2004**, *28*, 265–291.
- (48) Li, X.; Mullen, J. T.; Jin, Z.; Borysenko, K. M.; Buongiorno Nardelli, M.; Kim, K. W. *Phys. Rev. B* **2013**, *87*, 115418.
- (49) Cui, X.; Lee, G.-H.; Kim, Y. D.; Arefe, G.; Huang, P. Y.; Lee, C.-H.; Chenet, D. A.; Zhang, X.; Wang, L.; Ye, F.; Pizzocchero, F.; Jessen, B. S.; Watanabe, K.; Taniguchi, T.; Muller, D. A.; Low, T.; Kim, P.; Hone, J. *Nat. Nanotechnol.* **2015**, *10*, 534–540.
- (50) Baugher, B. W. H.; Churchill, H. O. H.; Yang, Y.; Jarillo-Herrero, P. *Nano Lett.* **2013**, *13*, 4212–4216.